Space Weather

RESEARCH ARTICLE
10.1029/2022SW003347

Daily Plasmaspheric TEC Variations From COSMIC GPS Observations Based on RBF Neural Network-Kriging Method

Qiqi Shi[1,2], **Shuanggen Jin**[1,3], **and Linlin Li**[1,2]

[1]Shanghai Astronomical Observatory, Chinese Academy of Sciences, Shanghai, China, [2]University of Chinese Academy of Sciences, Beijing, China, [3]School of Surveying and Land Information Engineering, Henan Polytechnic University, Jiaozuo, China

Key Points:

- A novel joint method is proposed to estimate the daily plasmaspheric total electron content (PTEC) model from COSMIC Global Positioning System observations
- Variation characteristics of the daily PTEC are investigated and obtained in terms of season, latitude, and longitude
- A good correlation between the daily PTEC and solar activity index is presented with up to 0.86

Correspondence to:

S. Jin,
sgjin@shao.ac.cn;
sg.jin@yahoo.com

Citation:

Shi, Q., Jin, S., & Li, L. (2023). Daily plasmaspheric TEC variations from COSMIC GPS observations based on RBF neural network-kriging method. *Space Weather*, *21*, e2022SW003347. https://doi.org/10.1029/2022SW003347

Received 16 NOV 2022
Accepted 10 JUL 2023

Author Contributions:

Conceptualization: Qiqi Shi, Shuanggen Jin
Data curation: Qiqi Shi
Formal analysis: Qiqi Shi, Shuanggen Jin, Linlin Li
Funding acquisition: Shuanggen Jin
Investigation: Qiqi Shi, Shuanggen Jin, Linlin Li
Methodology: Qiqi Shi
Software: Qiqi Shi
Supervision: Shuanggen Jin
Validation: Qiqi Shi
Writing – original draft: Qiqi Shi
Writing – review & editing: Qiqi Shi, Shuanggen Jin, Linlin Li

Abstract The low Earth orbit (LEO) satellite provides valuable direct observations for scientific investigation of the plasmasphere, while the plasmaspheric total electron content (PTEC) with a high temporal resolution cannot be precisely estimated due to fewer LEO satellites. In this paper, a novel joint method of radial basis function neural network—Kriging (RBF-Kr) method is designed to construct the daily PTEC model using the Constellation Observing System for Meteorology, Ionosphere and Climate Global Positioning System observations during the low (2009) and high (2013) solar activity years. Compared with the original RBF method, the RBF-Kr method reduces the mean absolute error and root mean square error from 0.77 to 0.60 TEC unit (TECU) and 0.99 to 0.80 TECU, respectively. The correlation coefficient (Corr) increased from 0.90 to 0.94. Furthermore, daily PTEC variations show that the PTEC at low latitudes is evenly distributed during equinox periods. The South American-Atlantic Ocean sector has a peak and trough in PTEC during the December and June solstices. A certain symmetrical distribution of PTEC is observed in the latitudinal direction, and the symcenter moves toward the summer hemisphere. The duration of extremal PTEC at 60°W is observed, which lasted up to more than 80 days around the December solstice. An obvious correlation between the solar flux and PTEC is found with up to 0.86, indicating that daily PTEC variations are mainly related to solar activities.

Plain Language Summary Due to the limited temporal-spatial resolution of observations, low Earth orbit (LEO) satellites cannot achieve the high temporal-spatial resolution plasmaspheric total electron content (PTEC) like the ground GPS estimated TEC. In order to improve the PTEC resolution further, we designed a novel joint method based on the neural network, and daily PTEC models for the low (2009) and high (2013) solar activity years were established using the Constellation Observing System for Meteorology, Ionosphere and Climate Global Positioning System data. The novel method has a better performance with higher accuracy than the original method in solving the insufficient coverage of daily models. In addition, daily PTEC variations are analyzed with the season, latitude, and longitude. Finally, by analyzing daily PTEC models with solar activity indices, a strong correlation is found between PTEC and solar flux.

1. Introduction

The ionosphere and plasmasphere are the upper parts of the atmosphere around the Earth. The ionosphere is about from 60 to 1,000 km, which is considered as a significant error source for the global navigation satellite system (GNSS) positioning and applications (e.g., Hernández-Pajares et al., 2011; Jakowski et al., 2011; Jin & Su, 2020). The plasmasphere is tightly attached to the upper ionosphere, extending from an altitude of the topside ionosphere to 3–5 times the Earth's radius. The plasmasphere contains relatively dense plasma with low energy, and the presence of electrons also affects the GNSS signal propagation and the upper Earth's space environment (e.g., Kotova, 2007). Therefore, effectively modeling and monitoring the plasmasphere are of vital importance to reveal the physical mechanism of the ionosphere-plasmasphere coupling and forecast the space weather.

Nowadays, a variety of observational techniques have emerged and developed, which provide abundant data to estimate the total electron content (TEC) over the Earth's atmosphere. Dual-frequency GNSS has been used extensively to extract the TEC from ground-based observations via the geometry-free (GF) combined observables or precise point positioning approach (e.g., Su et al., 2021; Zhang, 2016). Compared to the TEC extraction from ground-based GNSS observations, direct and indirect methods can be used to achieve the plasmaspheric TEC (PTEC) estimation. The direct method is to estimate slant TEC (STEC) along the signal's traveling path using

GPS receivers' observations onboard low Earth orbit (LEO) satellites at the appropriate altitude (e.g., Pedatella & Larson, 2010; Zhang et al., 2017). Receivers onboard LEO satellites can receive GPS signals for precise orbit determination (POD). Therefore, the PTEC along the GPS-LEO link can be obtained with the dual-frequency combined observables. As for the indirect method, the PTEC is calculated by subtracting the ionospheric TEC (ITEC) from the overall TEC. The ITEC can be estimated using integral calculation of electron density profiles in the corresponding altitude range. The electron density profiles are obtained by various methods, including ground-based ionosonde combined with the α-Chapman function (e.g., Belehaki et al., 2004), Constellation Observing System for Meteorology, Ionosphere and Climate (COSMIC) occultation (e.g., Cherniak et al., 2012; Habarulema et al., 2021; Panda et al., 2021), and Incoherent Scatter Radar (e.g., Chong et al., 2013).

The direct observation from the LEO satellite is the preferred method to monitor the plasmasphere. Yizengaw et al. (2008) used GPS observations onboard the JASON-1 satellite to calculate the PTEC by averaging, and investigated the relative contribution of the PTEC to the ground-based GPS TEC. Results indicated that the PTEC relatively contributed to ground-based GPS TEC most at night and least during the day. Shim et al. (2017) analyzed PTEC variations with mean PTEC values from the JASON-1 satellite during the years 2002–2008, and found the PTEC increased with the high solar flux, particularly for the equinox period. They examined that geomagnetic activity had little effect on the PTEC under low solar activity conditions, and the PTEC values at low latitudes decreased slightly with the increment of the geomagnetic activity during high solar activities. Additionally, the American sector exhibited a strong annual asymmetry with the highest and lowest PTEC values occurring during the December and June solstices. Chen et al. (2017) constructed a global plasmaspheric model from the COSMIC and Meteorological Operational (MetOp) GPS observations with the spherical harmonic function by 9×9 order to fit the vertical TEC (VTEC) per 4 hr. The PTEC map from only the COSMIC data was accurately validated by the MetOp-A data. Zhang, Liu, et al. (2016) established the annual and seasonal mean PTEC values in the geomagnetic coordinate system using the COSMIC data in the year 2008, which showed that the minimum PTEC value appears during the summer (May–August). The maximum and minimum PTEC values in diurnal variations occurred at around 12–14 magnetic local time (MLT) and 4–5 MLT, respectively. Jin et al. (2021) calculated PTEC maps using the monthly mean values in the geomagnetic coordinate system, and found that PTEC values showed a peak between 14:00 and 17:00 MLT and reached the lowest value between 3:00 and 6:00 MLT. In addition, a high correlation between monthly PTEC and the solar radio flux at 10.7 cm (F10.7) index was found from 2007 to 2017. Zhong et al. (2017) investigated the upward ionospheric TEC from the MetOp-A at 832 km orbital altitude and TerraSAR-X (TSX) at 520 km orbital altitude. The TEC data are split into grids with 5° (latitude) × 15° (longitude) under different seasons and solar activity conditions, and the median value in each grid is used as the map value. The longitudinal variations were analyzed in the topside ionosphere and plasmasphere at low latitudes, relating the geomagnetic dip angle and declination. Chen et al. (2019) constructed the PTEC model by griding the data into 5° (latitude) × 15° (longitude), and the median value in each grid was calculated for the map value under different seasons and solar activity conditions. The morphology of the Weddell Sea Anomaly (WSA) was mainly investigated. Results showed the WSA could also be observed in the plasmasphere, which was most prominent in winter under high solar activity.

The PTEC can be achieved directly from GPS observations onboard LEO satellites. One involves modeling PTEC in the zenith directions over a period of several hours using the spherical harmonic function. In this manner, the corresponding temporal resolution is 4 hr or more to establish a set of spherical harmonic coefficients. Nevertheless, negative PTEC values may occur at certain locations using this method, and the data processing is complicated. The other is to split grid points in the geomagnetic or geographic coordinate system, and use the mean or median value to represent the PTEC value at the plasmaspheric pierce point for a certain time interval. However, monthly, seasonal, or even annual interval was generally set to estimate and analyze PTEC variations over a long period. In order to improve the temporal resolution of the PTEC grid map described in the second method, we attempt to establish a daily PTEC model using COSMIC GPS observations. The daily PTEC model may have an issue with the lack of coverage. Therefore, specific spatial fitting is required to implement and estimate the daily PTEC model.

Since machine learning algorithms can be realized for the spatial fitting, a novel joint method of radial basis function (RBF) neural network-Kriging (RBF-Kr) is designed and carried out to establish daily PTEC models in this study. First, Section 2 introduces the COSMIC data source and methods to establish PTEC models. The method is validated and PTEC variations are analyzed in Section 3. Some discussions are presented in Section 4. Finally, conclusions are given in Section 5.

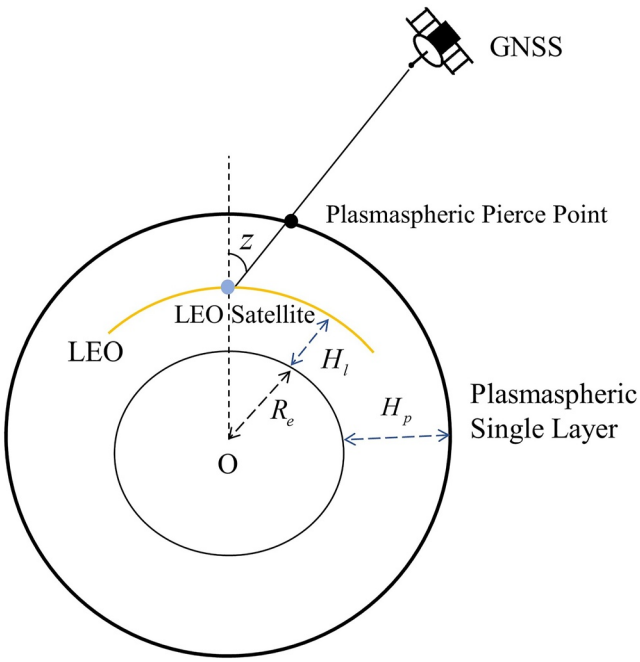

Figure 1. Diagram of plasmaspheric single layer VTEC estimation with the F&K geometric mapping function.

2. Data and Methods

2.1. Observation Data

Measurements from GPS receivers onboard LEO satellites provide a valuable opportunity to investigate the topside ionosphere and plasmasphere. As one of the representative GNSS radio occultation constellations of LEO satellites, the COSMIC-1 mission launched on 15 April 2006 consists of six LEO satellites with an orbital inclination of 72° at ~800 km orbital altitude. The onboard receiver of COSMIC satellites is equipped with four GPS antennas to track observation, including the GPS radio occultation for atmospheric/ionospheric profiling and observation for POD. The TEC datasets of GPS-LEO observations are obtained from the COSMIC Data Analysis and Archive Center (CDAAC). COSMIC-1 TEC data in this study were recorded in the level 1b products (podTec files) derived from the POD observations, including observation time, GPS/LEO satellites positions, and the absolute TEC along the ray path of the GPS-LEO link. To study the seasonal and daily variations of the PTEC throughout the year and related influence by solar activity, the podTec files under the conditions of the low (2009) and high (2013) solar activity years are collected from the COSMIC-1 data reprocessed in 2013. Moreover, we eliminate STEC values <0 TEC unit (TECU, 1 TECU = 10^{16} el/m^2) or >60 TECU to avoid gross errors and set the cut-off elevation as 30° to reduce the impact of mapping function (MF) errors. The sampling interval of original data in podTec files is 1 s, and observations with a time interval of 10 s are extracted to reduce nearby similar observations.

2.2. Estimation of Daily PTEC

The dual-frequency observations of GPS receivers onboard LEO satellites are implemented with the carrier-to-code leveling (CCL) method to estimate the TEC and the differential bias (DCB). The GPS satellite DCB is calibrated using the Center for Orbit Determination in Europe (CODE) products. The spherical symmetry assumption is adopted to estimate the TEC, and detailed descriptions are available in the earlier study (Yue et al., 2011). TEC products provided by the CDAAC are the absolute STEC, in which DCBs of satellites and receivers have been corrected. Then, the STEC is converted to the VTEC by a MF. The F&K geometric MF proposed by Foelsche and Kirchengast (2002) is adopted in this paper, and its diagram is depicted in Figure 1. Compared with the single-layer MF used by ground-based observations, the F&K geometric MF shows a more reasonable performance in STEC-VTEC conversion for the GPS-LEO link (e.g., Zhong et al., 2016), which can be expressed as follows:

$$M_{F\&K}(z) = \frac{1 + R}{\cos z + \sqrt{R^2 - (\sin z)^2}} \quad (1)$$

$$R = \frac{R_e + H_p}{R_e + H_l} \quad (2)$$

where z refers to the zenith angle, R_e is the average radius of the Earth, H_l is the orbit altitude of LEO satellites, H_p is the altitude of the plasmaspheric single layer or plasmaspheric pierce point. Here it is set to 3,000 km, which is same as the data processing in the CDAAC as given by Yue et al. (2011).

Figure 2 shows the geographical distribution of GPS-COSMIC plasmaspheric pierce points on 18 March 2009, day of year 077. Plasmaspheric pierce points show inadequate coverage in the Arctic and Antarctic regions. Hence, latitudinal and longitudinal ranges are set from 70°N to 70°S and 180°W to 180°E, respectively. PTEC values are assigned into grids of 2.5° × 5° (latitude vs. longitude) with a span of 1 day. The full-year data coverages of the daily global plasmaspheric map in 2009 and 2013 are shown in Figure 3. The coverages vary between 80% and 90% on most days. Plasmaspheric pierce points on a single day have no complete coverage over all grid points due to the data volume limitation, data preprocessing, and grid division. In order to ensure the reliability of the subsequent spatial fitting, data with coverage above 70% are used to establish daily PTEC models.

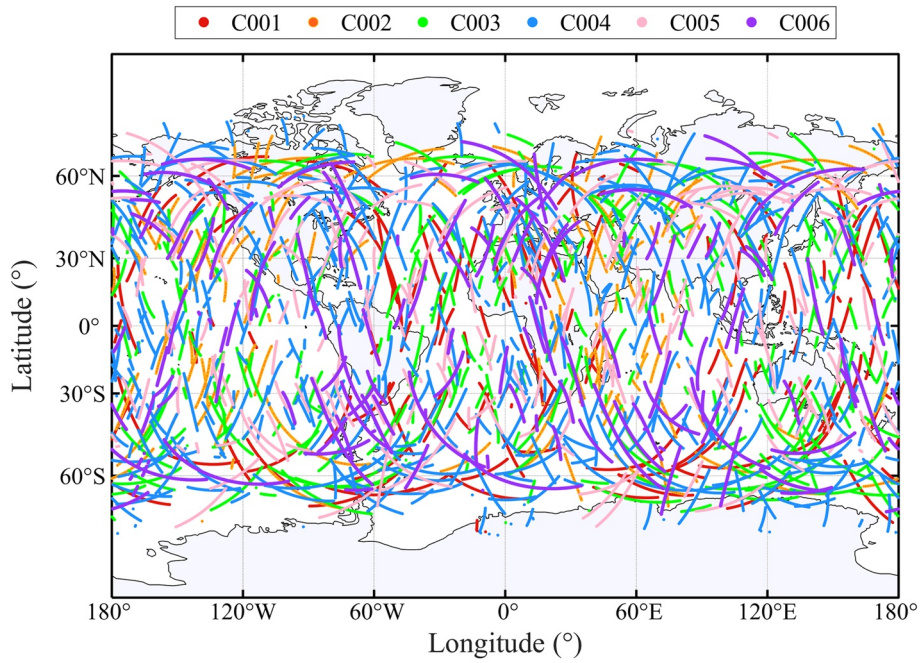

Figure 2. Distribution of GPS-COSMIC plasmaspheric piercing points on 18 March 2009 (day of year 077). C001 ~ C006 represent six COSMIC low Earth orbit satellites.

2.3. RBF Neural Network—Kriging

The daily PTEC model requires a spatial fitting method for filling and smoothing data. The RBF neural network is chosen as the basic processing method because of significant advantages such as high flexibility, learning ability, and approximate arbitrary continuous functions (e.g., He & Zhao, 2018; Lazzaro & Montefusco, 2002). The RBF neural network consists of three layers: (a) an input layer with multiple nodes, which is suitable for multivariable input; (b) a hidden layer with multiple neurons, in which the number of neurons can be dynamically adjusted to satisfy the fitting need; (c) an output layer with one or several nodes. The RBF neural network is a special form of the back propagation neural network, except that the activation function uses RBF in the hidden layer. A RBF is a real-valued function, and its value depends only on the distance from the origin. The hidden layer based on the mapping relation by the RBF is connected with the input layer and no longer requires the weight value. The Gaussian activation function in RBF neural network can be written as (e.g., Deng et al., 2021; Moody & Darken, 1989):

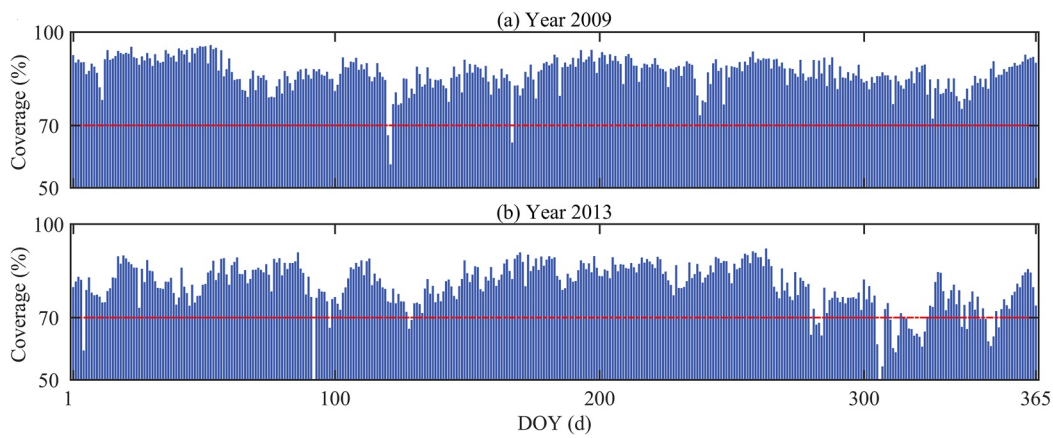

Figure 3. Data coverage of the daily global plasmaspheric map in 2009 and 2013. The red horizon dashed line represents the coverage equaling to 70%.

$$\varphi_i(x) = \exp\left(-\frac{1}{2\sigma_i}\left\|x - c_i\right\|^2\right) \tag{3}$$

where x is the input vector, c_i and σ_i the center and spread of the ith RBF node, $\|x - c_i\|$ is the Euclidian distance function. The spread constant σ was set to 0.1, which can be adjusted according to the specific data distribution and characterization. Once the activation function of the hidden layer is determined, the output of the RBF neural network can be calculated by the linear combination as:

$$y_r = \sum_i^m w_i \cdot \varphi_i(x) \tag{4}$$

where w_i is the weight vector of the output layer, and m denotes the number of neurons in the hidden layer. As a supervised training algorithm, a residual vector v_r can be determined based on the RBF neural network output of the training set:

$$v_r = y_o - y_r \tag{5}$$

where y_o represents the actual observed output.

In addition, the estimated PTEC models based on RBF neural networks maintain continuous and smooth at adjacent positions. The distribution of residuals at adjacent points is also correlated to some extent. Therefore, we attempt to use a residual distribution fitted with the Kriging method as a correction to the original RBF neural network. The corresponding concept is consistent with the direct neural network residual Kriging (e.g., Kanevsky et al., 1996; Seo et al., 2015): 1. Using the artificial neural networks to achieve the overall non-linear spatial estimation. 2. Applying a geostatistical methodology for residuals to implement the local spatial approximation. The Kriging method considers spatial autocorrelation and employs a semivariogram as a measure of spatial variability. The semivariogram is calculated by (e.g., Munyati & Sinthumule, 2021; Takka et al., 2018):

$$\gamma(h) = \gamma_{i,j} = \frac{1}{2}E\left[(Z_i - Z_j)^2\right] \tag{6}$$

where h is the separation distance between sample points, and Z denotes the spatial variable at the sample point. During the processing of experimental data, the semivariogram is generally represented using a theoretical model. In this paper, the spherical model is chosen to characterize the relationship between the semivariogram γ and distance h:

$$\gamma(h) = \begin{cases} 0 & h = 0 \\ C_0 + C\left(\frac{3}{2}\cdot\frac{h}{a} - \frac{1}{2}\cdot\frac{h^3}{a^3}\right) & 0 < h \le a \\ C_0 + C & h > a \end{cases} \tag{7}$$

where a represents the effective range; C_0 and C are the nugget and partial sill, respectively. The parameters in the theoretical model need to be estimated in the experimental data processing. Based on the ordinary kriging method, the spatial variables v of the unsampled points can be given (e.g., Oliver & Webster, 1990):

$$v = \sum_i^n \lambda_i \cdot Z_i \tag{8}$$

where λ is the Kriging weight coefficient calculated by solving the following linear system with γ, and the details of the implementation can be found in the previous study (Takka et al., 2018).

According to the above description, a novel joint (RBF-Kr) method was designed and implemented for the daily PTEC model, and the flowchart is shown in Figure 4. Using the grid PTEC data in Section 2.2 as the data set, the entire data set is randomly split into a training set (80%) a validation set(10%), and a test set (10%) per day. The input features are the latitude and longitude with the linear normalization (Min-Max, 0–1), and the output is the PTEC value at the grid position. The training process is dynamically regulated by adjusting the number of neurons in the hidden layer, and the validation set is used to revent overfitting. The solution method of the

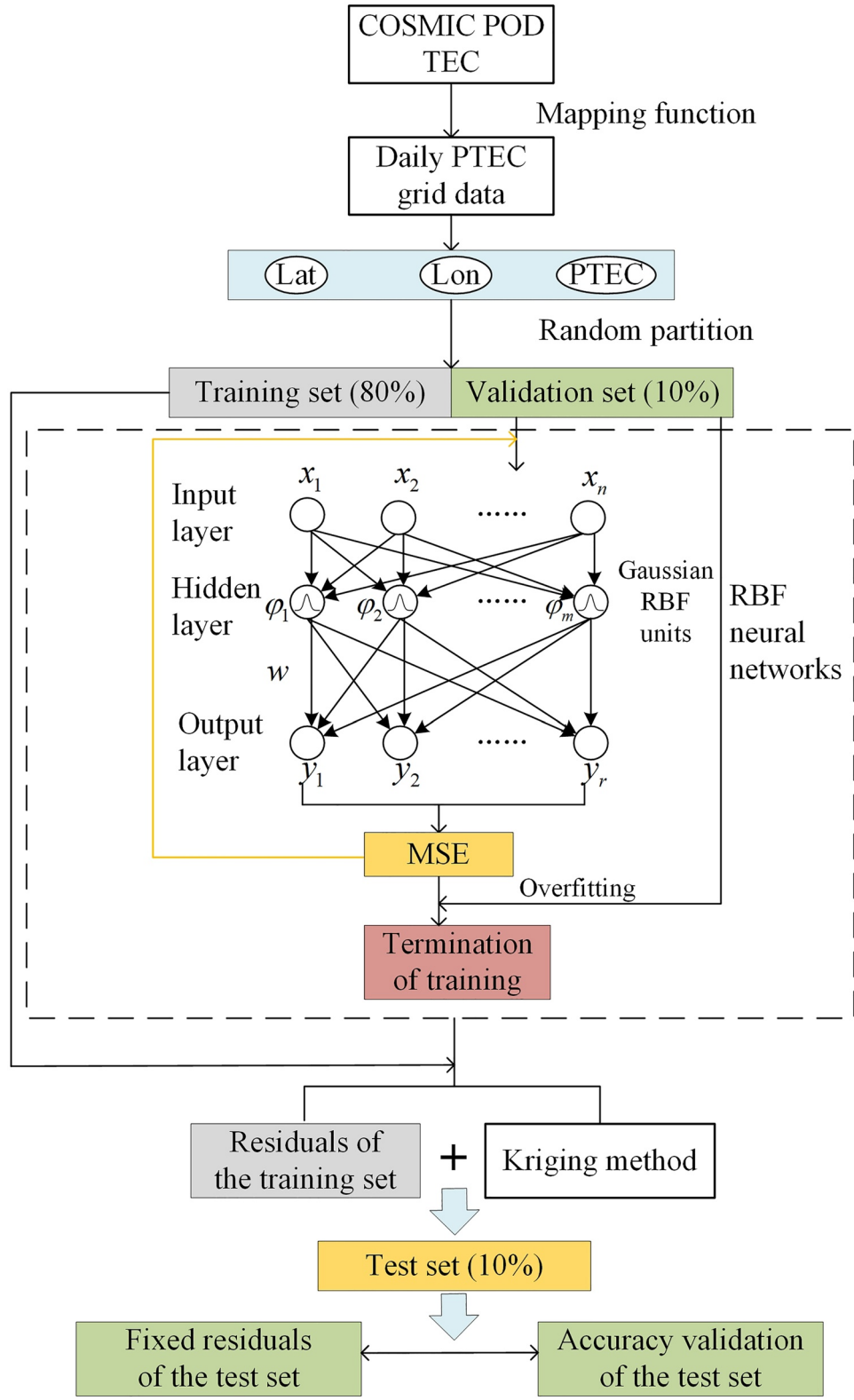

Figure 4. Flowchart of the daily plasmaspheric total electron content model based on the RBF-Kr method.

Table 1
Multiple Indicators of Radial Basis Function and RBF-Kr Methods for the Spatial Fitting During Testing Periods

		MAE (TECU)			RMSE (TECU)			Corr		
Year	Method	Max	Min	Mean	Max	Min	Mean	Max	Min	Mean
2009	RBF	0.95	0.56	0.74	1.22	0.72	0.95	0.92	0.73	0.85
	RBF-Kr	0.74	0.43	0.58	0.98	0.57	0.76	0.95	0.80	0.91
2013	RBF	0.99	0.66	0.81	1.28	0.86	1.03	0.93	0.80	0.88
	RBF-Kr	0.83	0.50	0.64	1.03	0.68	0.84	0.96	0.86	0.92

RBF neural network is based on the least squares algorithm to estimate the weights between the hidden layer and output layer (e.g., Niros & Tsekouras, 2012). Daily data are used as one modeling process, including the model input, output, residual correction, and test validation. Finally, the daily PTEC models are estimated based on RBF and RBF-Kr methods in 2009 and 2013, excluding the data for the deleted days.

3. Results and Analysis

3.1. Accuracy Evaluation

In order to validate the effectiveness of the RBF-Kr method, the accuracy of the spatial fitting is analyzed using multiple indicators of the mean absolute error (MAE), root mean square error (RMSE), and correlation coefficient (Corr) as follows:

$$\mathrm{MAE} = \frac{1}{N}\sum_{i=1}^{N}\left|\mathrm{PTEC}_f^i - \mathrm{PTEC}_o^i\right| \tag{9}$$

$$\mathrm{RMSE} = \sqrt{\frac{1}{N}\sum_{i=1}^{N}\left|\mathrm{PTEC}_f^i - \mathrm{PTEC}_o^i\right|^2} \tag{10}$$

$$\mathrm{Corr} = \frac{\sum_{i=1}^{N}\left(\mathrm{PTEC}_f^i - \overline{\mathrm{PTEC}}_f\right)\left(\mathrm{PTEC}_o^i - \overline{\mathrm{PTEC}}_o\right)}{\sqrt{\sum_{i=1}^{N}\left(\mathrm{PTEC}_f^i - \overline{\mathrm{PTEC}}_f\right)^2}\sqrt{\sum_{i=1}^{N}\left(\mathrm{PTEC}_o^i - \overline{\mathrm{PTEC}}_o\right)^2}} \tag{11}$$

where PTEC_f^i and PTEC_o^i represent the spatial fitted and observed PTEC, respectively, $\overline{\mathrm{PTEC}}_f$ and $\overline{\mathrm{PTEC}}_o$ are the corresponding mean PTEC values. These indicators, that is, maximum, minimum, and mean values, are utilized for the comparison of different methods.

We implemented RBF and RBF-Kr methods to establish daily PTEC models in 2009 and 2013. The performance of the methods is shown in Table 1. Both methods have certain reliability with MAE and RMSE values below 1.00 and 1.30 TECU. In particular, the RBF-Kr method keeps the MAE and RMSE below 1.10 TECU, which improves the accuracy somewhat compared to the original method. Mean Corr values using the two methods are above 0.85, and the RBF-Kr method has a better performance with mean Corr values above 0.91, indicating a strong correlation between fitted and observed PTEC. The results for the high solar activity year (2013) are slightly worse in the MAE and RMS, probably due to the significant plasmaspheric variations under high solar activity conditions. To examine the relationship between fitted and observed PTEC, scatter diagrams are provided in Figure 5. The daily PTEC values of the test set vary within 20 TECU, and the scatter points are primarily located near the baseline. The red line is closer to the baseline employing the RBF-Kr method.

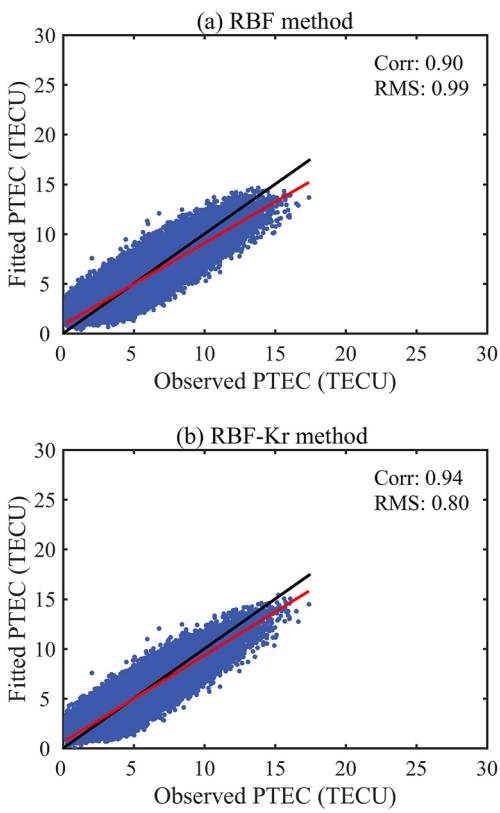

Figure 5. Scatter diagrams of the correlation between observed and fitted plasmaspheric total electron content values using (a) radial basis function and (b) RBF-Kr methods. The black and red lines represent the baseline and fitted line, respectively.

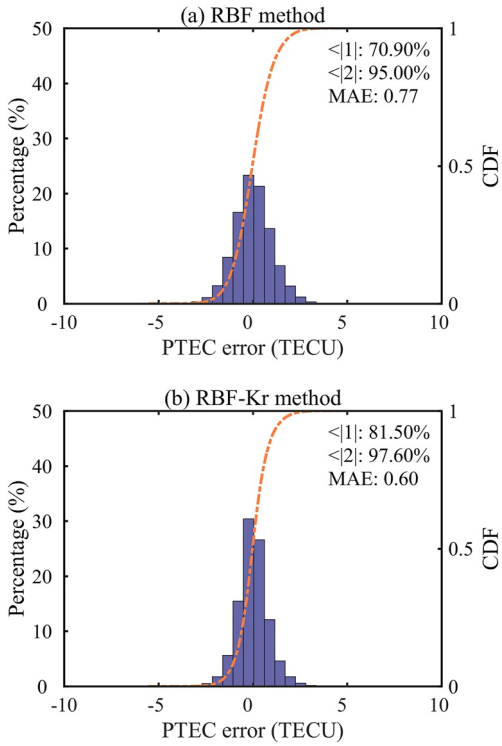

Figure 6. Distributions of plasmaspheric total electron content (PTEC) errors between observed and fitted PTEC values using (a) radial basis function and (b) RBF-Kr methods. The orange dashed lines represent the CDFs.

The distributions of PTEC errors between observed and fitted PTEC values for the two methods are depicted in Figure 6. It can be clearly observed that PTEC errors of both methods are broadly distributed around zero. The distribution of the PTEC error using the RBF-Kr method has a better performance within |1| TECU, and the proportion of quantitative distribution increases from 70.90% to 81.50%. However, the proportion of the PTEC error only increases from 95.00% to 97.60% within |2| TECU. Compared with the RBF method, the cumulative distribution function of the RBF-Kr method shows an obvious ascent within |1| TECU. The CDFs show the number of PTEC errors is small minority above |2| TECU, which are infinitely close to the coordinate box lines in this range. After analyzing various perspectives from statistical indicators and error distributions, the RBF-Kr method shows a robust performance and effective improvement for the daily PTEC model.

3.2. Seasonal PTEC Variations

The daily PTEC time series from the RBF-Kr method are analyzed for PTEC variation characteristics. We separated every year into four seasonal periods approximately centered on an equinox or solstice. One-half of the interval time between the adjacent solstice and equinox was set the duration before and after the solstice or equinox. In order to investigate the general differences in the global distribution, the mean PTEC values are calculated under different seasons. Figure 7 shows global plasmaspheric maps during the different periods of equinoxes and solstices under the low (2009) and high (2013) solar activity conditions. The PTEC at low latitudes shows a symmetrical distribution along the magnetic equator, and each season appears the same pattern with a bright band along the magnetic equator. Demarcated by the magnetic equator, the PTEC values are decreased with the increment of the latitude. PTEC values are overall greater in the high solar activity year than in the low year. In the equinox periods, the distribution of PTEC shows no significant differences in the longitudinal direction. In contrast to the equinox periods, the South American-Atlantic Ocean sector shows an obvious PTEC minimum value during the June solstice period. The characteristic of the minimum PTEC values is evident in the low solar activity year. For the December solstice period, the South American-Atlantic Ocean sector shows the PTEC maximum values instead, which exhibits an annual variation. During the December solstice period, the PTEC extremal region spreads significantly along the magnetic equator toward the African sector with high solar activity.

To investigate the consistency between daily and general seasonal PTEC variations, the daily global plasmaspheric maps for the days of equinoxes and solstices are depicted in Figure 8. On the days of the equinoxes, the distribution of PTEC maximum values are distributed along the magnetic equator of the Earth at low latitudes, and there is no significant difference in the PTEC between the northern and southern hemispheres. The plasmasphere has multiple PTEC peaks at low latitudes in the daily PTEC model on the equinoxes. For the solstices, the PTEC values are significantly higher in the summer hemisphere than in the winter hemisphere. The bright band at low latitudes along the magnetic equator is moved toward the summer hemisphere. During the solstices of June and December, the South American sector exhibits the PTEC minimum and maximum values, respectively. The increment in PTEC is not as significant, with only 3–5 TECU increasing in the high solar activity. Compared with the low activity year, the peak of the South American sector spreads to the sides along the magnetic equator on the December solstice. The phenomenon appears remarkably in the high solar activity year, particularly in the African sector. The seasonal PTEC variations on the day of the equinoxes and solstices are consistent with the general seasonal variations, but more local differences and variations can be seen in daily PTEC maps.

3.3. Latitudinal and Longitudinal PTEC Variations

In this section, latitudinal and longitudinal PTEC variations are analyzed using global PTEC maps. Figure 9 presents the distributions in the latitudinal direction of the PTEC averaged along the longitude during the low (2009) and high (2013) solar activity years. Overall, the PTEC distribution is basically symmetrical around the

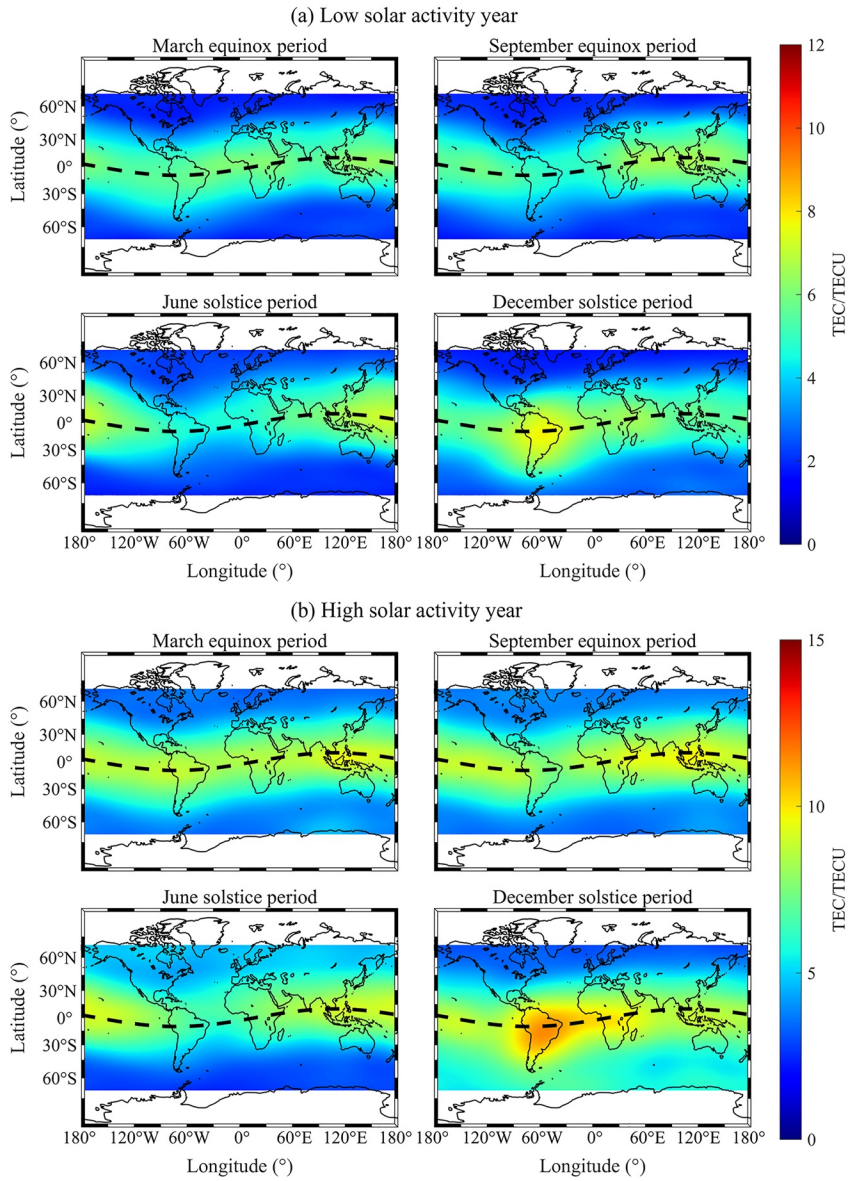

Figure 7. Seasonal variations of global plasmaspheric maps during the March equinox period, September equinox period, June solstice period, and December solstice period for the low solar activity year 2009 (a) and high solar activity year 2013 (b). The black dashed line represents the position of the Earth's magnetic equator.

peak in latitude for each season. The maximum PTEC values in latitudes are around 0° during the equinox period, but the maximum values are shifted toward the corresponding summer hemisphere during the solstice periods. During the December solstice period, the maximum PTEC values are 6.24 and 9.38 TECU in the low and high solar activity conditions, respectively, and the mean values are also shown with the largest. The fluctuations in the summer hemisphere are more significant than those in the winter hemisphere during the solstice periods. Moreover, PTEC fluctuations are more noticeable under the high solar activity year from the width of the shadow area. Due to the influence of the extreme PTEC in the December solstice period, the fluctuations of PTEC values are pronounced in the southern hemisphere under the high solar activity condition. Its influence may also be present at the end of the September equinox period.

We can clearly see the extremal PTEC during the June and December solstice periods, which is located in the American-Atlantic sector. Hence, the daily PTEC variations at 60° W (the American-Atlantic sector) are given in Figure 10, and the characteristics of the extremal region are analyzed. Centered on the December solstice, the maximum PTEC values of the regions at 60° W exceed 10.00 TECU, which covers the lower latitudes of the

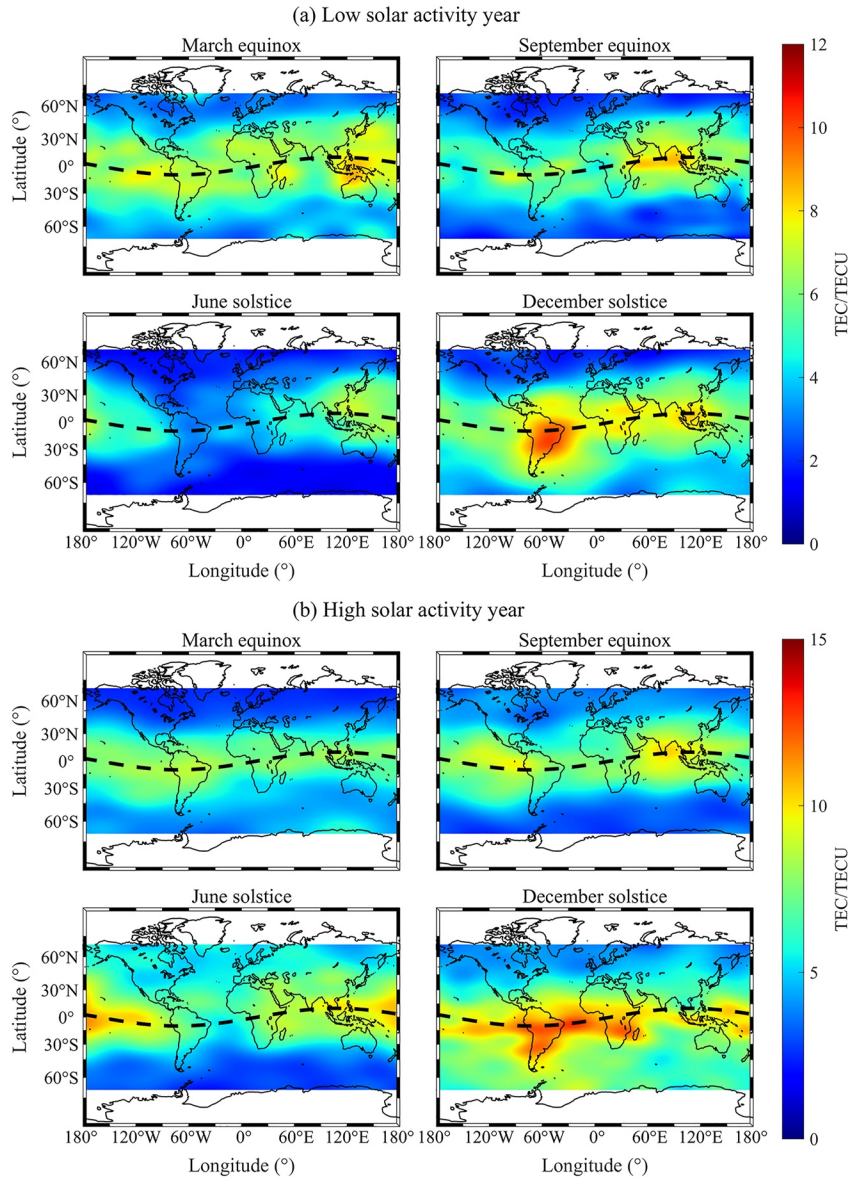

Figure 8. Daily global plasmaspheric maps on the days of the March equinox, September equinox, June solstice, and December solstice during the low solar activity year 2009 (a) and high solar activity year 2013 (b).

northern hemisphere and mid-low latitudes of the southern hemisphere. It can be observed that the PTEC exhibit lower values in the period from around the June solstice to the September equinox. The extremal regions at 60° W lasted over 80 days and began to weaken as approaching the March equinox. There are some differences in the start and end times for the 2-year duration. In the high solar activity year, the extremal PTEC may occur earlier at the end of the September equinox period. In addition to longitudinal variations due to seasonal and geomagnetic influences, the increment in PTEC because of the solar radiation also affects the plasmasphere.

3.4. PTEC Variations With Solar Activities

The solar radiation is the main energy source in the Earth's atmosphere and has an importance influence on electron density variations. Here, we choose the F10.7 index as the measurement of the solar activity condition. The mean values of daily PTEC models are calculated to investigate the correlation with the F10.7 index. Figure 11 depicts the distribution and correlation between the PTEC and F10.7 index. For the low solar activity year, the F10.7 indices are below 90 sfu, and minor changes in PTEC are over the corresponding period. In the high activity

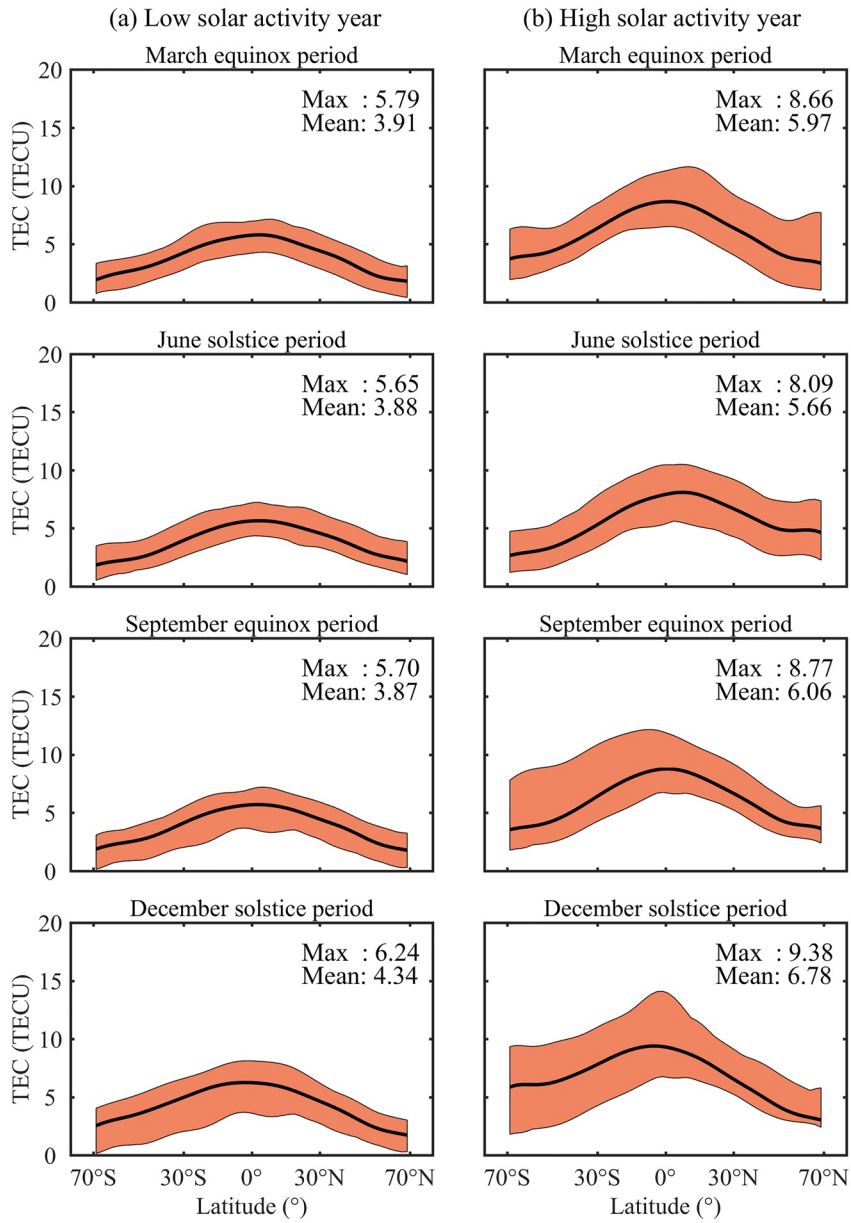

Figure 9. Distributions in the latitudinal direction of the daily plasmaspheric total electron content (PTEC) values averaged along the longitude during the low solar activity year 2009 (a) and high solar activity year 2013 (b). The black line represents the mean PTEC value during the corresponding period, and the shaded area represents the PTEC fluctuation range (where the "Max" values represent the maximum values of the mean line in black).

year, a clear consistency was found between apparent solar flux changes and PTEC fluctuations. Figure 11 (c) shows the Corr of 0.86, which indicates a strong correlation between the daily mean PTEC values and F10.7 indices. However, the PTEC has a dense distribution during the period of low solar radiation (2009) and increases with the F10.7 index later under the high solar radiation (2013). Moreover, Lee et al. (2013) described that the ITEC and PTEC increased almost linearly and nearly logarithmically with increasing solar activities, respectively. Our 2 years of data fit both the beginning and rising periods of the logarithmic distribution.

4. Discussion

The RBF-Kr method has a better performance in the MAE and RMS, with an improvement by 22.08% and 19.19%. However, the distribution of PTEC errors shows that the improvement within |2| TECU is only increased

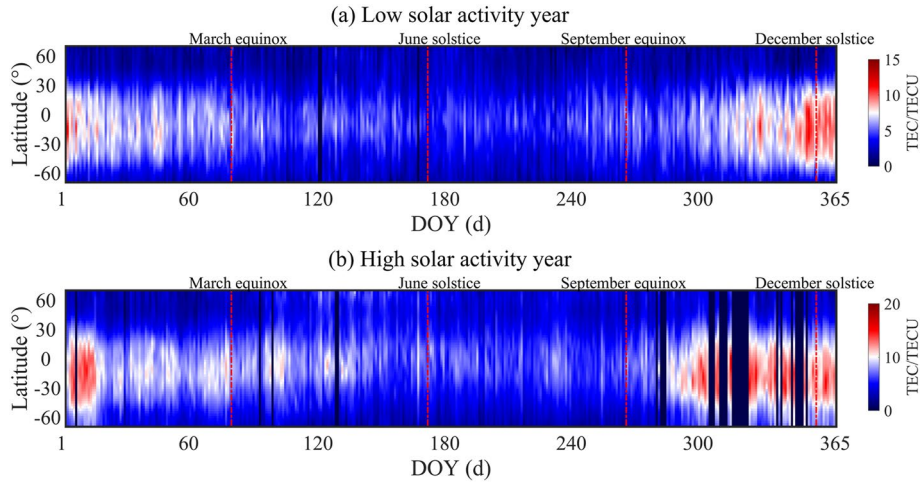

Figure 10. Daily plasmaspheric total electron content variations at 60° W throughout the low solar activity year 2009 (a) and high solar activity year 2013 (b). The black strips represent the deleted data (the data coverage is less than 70%).

from 95.00% to 97.60% for the test set in Figure 6. Table 2 provides the proportional distribution of the residuals in the training set. The residual correction from the Kriging method based on the training set leads to a relatively small proportional amount of the larger errors, and the size of the correction is also hardly noticeable. It shows that the method can give a holistic correction to improve the accuracy of the spatial fitting, and a slight amount of large deviations or gross errors can be effectively resisted without affecting the overall accuracy.

The global distribution of PTEC is characterized by an apparent bright band along the magnetic equator at low latitudes, while the mid-high latitudes are generally smoother with low PTEC values. The plasma in the plasmasphere is obtained mainly by upward transporting from the ionosphere. There is a tight diffusion and exchange driven by the O^+ and H^+ between the topside ionosphere and plasmasphere (e.g., Gulyaeva & Bilitza, 2012). Figure 12 shows the distribution of the mean PTEC values in the geomagnetic coordinate system using the PTEC data during the years 2009 and 2013. PTEC values in the high solar activity year (2013) are significantly greater than that in the low solar activity year (2009), but the spatial distribution is similar in both years. The maximum PTEC values occur at around 14 MLT during the day, while the minimum PTEC values occur at 4 ~ 6 MLT. The diurnal variation is mainly due to the following reason: During the day, ions in the ionosphere are drifted and diffused upwards along geomagnetic field lines into the plasmasphere. Then ions are returned to replenish the ionosphere at night. However, the ionized components of the ionosphere are considerably less present in the mid-high latitudes, leading to a thin plasmasphere.

The diurnal variations of PTEC have been extensively and adequately examined. In this study, we mainly focus on continuous variations and fluctuations of the PTEC globally based on daily values. The PTEC at low latitudes is uniformly spreading throughout the magnetic equator during the equinox periods. During the above periods,

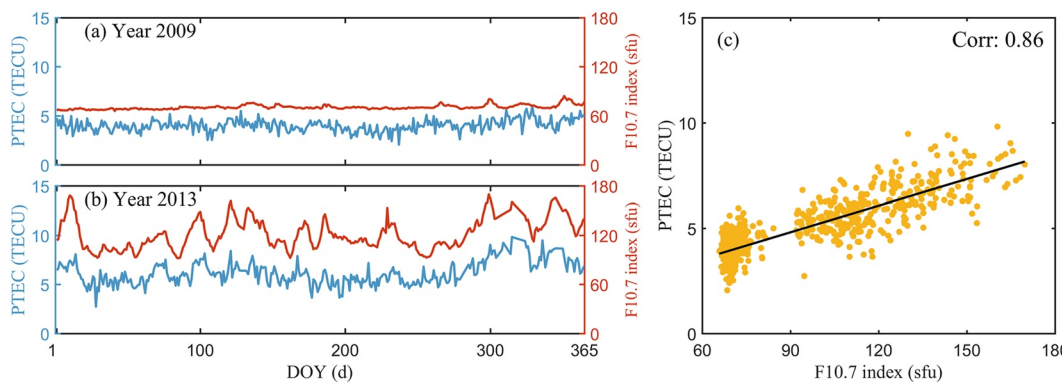

Figure 11. Distribution of the plasmaspheric total electron content (PTEC) and F10.7 indices in 2009 (a) and 2013 (b), and the scatter diagram (c) of the correlation between PTEC and F10.7 index. The black line represent the fitted line.

Table 2
Proportion of Residuals in the Training Set

Range (TECU)	<|1|	|1|~|2|	|2|~|4|	>|4|
Proportion (%)	72.75	23.16	4.07	<0.02

there was also no noticeable difference in the distribution of the PTEC in the northern and southern hemispheres. As for solstice periods, the PTEC is noticeably higher in the summer hemisphere than in the winter hemisphere due to solar radiation. Besides, a clear peak and bottom are visible in the South American-Atlantic Ocean sector during the December and June solstices. Figure 13 shows the distribution of the geomagnetic inclination at 3,000 km altitude in 2009 calculated by the International Geomagnetic Reference Field (IGRF) (Alken et al., 2021). In particular, the PTEC distribution in the South American-Atlantic Ocean sector is nearly consistent with the geomagnetic inclination. There is a significant offset of the geomagnetic inclination to the south at this location. The geomagnetic field orientation can be regarded as a dominant factor in the PTEC distribution. The above phenomenon has been observed in previous studies, but the physical mechanism was not known. The longitudinal variations may be comprehensively influenced by the longitudinal asymmetry of the geomagnetic field line footprint distribution, plasma source controlled by solar radiation, and the equatorward neutral winds combined with the geomagnetic field orientation (e.g., Kashcheyev & Nava, 2019; Pedatella et al., 2011; Zhong et al., 2017). Moreover, the spatial physical process is a basis for explaining the distribution and variation of spatial PTEC data. The physical processes of the coupling and exchange between the ionosphere and the plasmasphere need to be further studied. The physical mechanisms underlying the influence of seasonal variations on the duration of extreme regions still require further research.

5. Conclusions

GNSS observations on LEO satellites can monitor and investigate the PTEC variations. However, the temporal resolution of PTEC estimation from LEO satellites needs to be enhanced because of the low LEO satellite coverage and temporal resolution. In order to establish the daily PTEC model, we proposed and implemented a novel joint method called RBF-Kr in this study. After evaluating the accuracy of the RBF-Kr method, daily PTEC models were constructed in the low solar activity year (2009) and high solar activity year (2013), and a comprehensive investigation of PTEC variations with respect to the season, latitude, and longitude was conducted. The main results and conclusions are summarized as follows:

1. Compared with the original RBF neural network, the RBF-Kr method has a better performance in terms of precision and effectiveness for estimating the daily PTEC. The MAE, RMSE, and Corr in 2 years are from 0.77 TECU, 0.99 TECU, and 0.90 to 0.60 TECU, 0.80 TECU, and 0.94, respectively.
2. An imperfectly symmetrical PTEC distribution was shown in the latitudinal direction along the equator, whose peaks move to the summer hemisphere. Fluctuations are significantly higher in the summer hemisphere than in the winter hemisphere. The PTEC values and fluctuations in the high solar activity year are more obvious than those in the low solar activity year.
3. The extremal PTEC region at 60° W was observed with more than 80 days distributed around solstices. However, there are some differences in starting and ending times for the 2-year durations of the extremal region. Furthermore, an obvious correlation between daily PTEC values and solar activities was found with up to 0.86, indicating that daily PTEC variations are mainly related to solar activities.

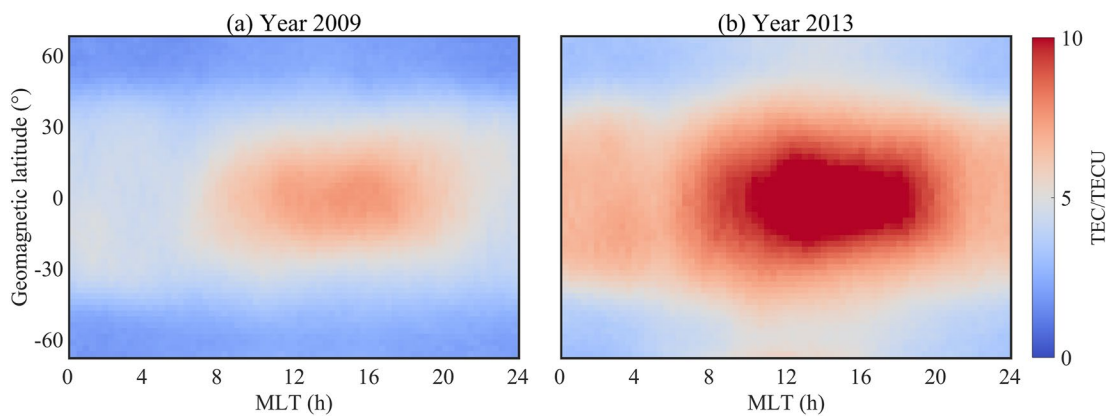

Figure 12. Distributions of the mean plasmaspheric total electron content values during the low solar activity year 2009 (a) and high solar activity year 2013 (b).

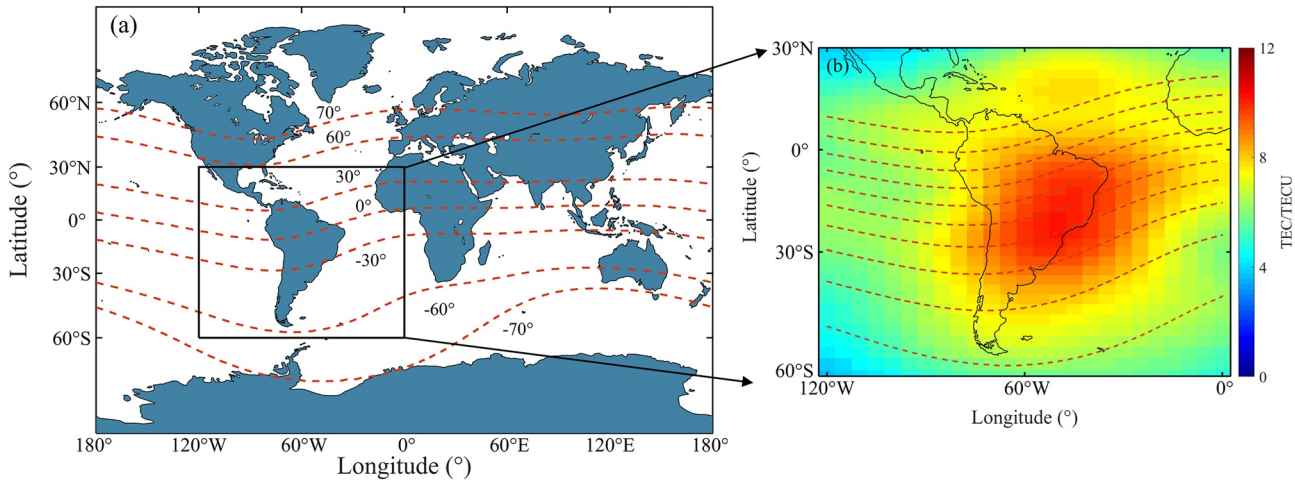

Figure 13. Distribution of the geomagnetic inclination at 3,000 km altitude in 2009, which located in the global area (a) and South American-Atlantic Ocean sector (b). The red dashed line represents the contour line of the geomagnetic inclination. The range in (b) is between −60° and 30° with the 10° interval and the plasmaspheric total electron content model is on the day of the December solstice in 2009.

LEO satellites play a significant role in directly observing the plasmasphere. To enable adequate investigations of the plasmaspheric variations accompanied by the COSMIC-2, Fengyun (FY), and MetOp satellites, more spatial data and PTEC variations with a long-time span will be carried out in the future, as well as their physical mechanisms.

Data Availability Statement

COSMIC GPS observations are available from the University Corporation for Atmospheric Research CDAAC (CDAAC, 2022). The F10.7 index can be obtained from the NASA' Goddard Space Flight Center (Goddard Space Flight Center, 2023). The IGRF code can be downloaded from the web page hosted at the National Oceanic and Atmospheric Administration/National Centers for Environmental Information (NOAA/NCEI) (IAGA, Alken et al., 2021). The daily PTEC models produced from this work are available from the repository figshare (Shi et al., 2023).

Acknowledgments

This work was supported by the National Natural Science Foundation of China (NSFC) Project (Grant12073012). The authors thanked the CDAAC for providing COSMIC GPS observations and the National Aeronautics and Space Administration (NASA)'s Goddard Space Flight Center for providing the F10.7 index. We also thanked the International Association of Geomagnetism and Aeronomy (IAGA) for providing the IGRF.

References

Alken, P., Thébault, E., Beggan, C. D., Amit, H., Aubert, J., Baerenzung, J., et al. (2021). International geomagnetic reference field: The thirteenth generation [Software]. Earth Planets and Space, *73*, 49. https://doi.org/10.1186/s40623-020-01288-x

Belehaki, A., Jakowski, N., & Reinisch, B. W. (2004). Plasmaspheric electron content derived from GPS TEC and digisonde ionograms. *Advances in Space Research*, *33*(6), 833–837. https://doi.org/10.1016/j.asr.2003.07.008

CDAAC (2022). COSMIC GPS observations [Dataset]. CDAAC. https://doi.org/10.5065/ZD80-KD74

Chen, P., Li, Q., Yao, Y., & Yao, W. (2019). Study on the plasmaspheric Weddell Sea Anomaly based on COSMIC onboard GPS measurements. *Journal of Atmospheric and Solar-Terrestrial Physics*, *192*, 104923. https://doi.org/10.1016/j.jastp.2018.09.012

Chen, P., Yao, Y., Li, Q., & Yao, W. (2017). Modeling the plasmasphere based on LEO satellites onboard GPS measurements. *Journal of Geophysical Research: Space Physics*, *122*(1), 1221–1233. https://doi.org/10.1002/2016JA023375

Cherniak, I. V., Zakharenkova, I. E., Krankowski, A., & Shagimuratov, I. I. (2012). Plasmaspheric electron content derived from GPS TEC and FORMOSAT-3/COSMIC measurements: Solar minimum condition. *Advances in Space Research*, *50*(4), 427–440. https://doi.org/10.1016/j.asr.2012.04.002

Chong, X., Zhang, M., Zhang, S., Wen, J., Liu, L., Ning, B., & Wan, W. (2013). An investigation on plasmaspheric electron content derived from ISR and GPS observations at Millstone Hill. *Chinese Journal of Geophysics (in Chinese)VL -*, *56*(3), 738–745. https://doi.org/10.6038/cjg20130303

Deng, Y., Zhou, X., Shen, J., Xiao, G., Hong, H., Lin, H., et al. (2021). New methods based on back propagation (BP) and radial basis function (RBF) artificial neural networks (ANNs) for predicting the occurrence of haloketones in tap water. *Science of the Total Environment*, *772*, 145534. https://doi.org/10.1016/j.scitotenv.2021.145534

Foelsche, U., & Kirchengast, G. (2002). A simple "geometric" mapping function for the hydrostatic delay at radio frequencies and assessment of its performance. *Geophysical Research Letters*, *29*(10), 111-111–111-114. https://doi.org/10.1029/2001GL013744

Goddard Space Flight Center. (2023). The F10.7 index [Dataset]. Goddard Space Flight Center. Retrieved from https://spdf.gsfc.nasa.gov/pub/data/omni/low_res_omni/

Gulyaeva, T. L., & Bilitza, D. (2012). Towards ISO standard Earth ionosphere and plasmasphere model. In R. J. Larsen (Ed.), *New developments in the standard model* (pp. 1–39). NOVA.

Habarulema, J. B., Okoh, D., Bergeot, N., Burešová, D., Matamba, T., Tshisaphungo, M., et al. (2021). Interhemispheric comparison of the ionosphere and plasmasphere total electron content using GPS, radio occultation and ionosonde observations. *Advances in Space Research*, *68*(6), 2339–2353. https://doi.org/10.1016/j.asr.2021.05.004

He, T., & Zhao, K. (2018). Multispectral remote sensing land use classification based on RBF Neural network with parameters optimized by genetic algorithm. In *Paper presented at 2018 international conference on sensor networks and signal processing (SNSP)*.

Hernández-Pajares, M., Juan, J. M., Sanz, J., Aragón-Àngel, À., García-Rigo, A., Salazar, D., & Escudero, M. (2011). The ionosphere: Effects, GPS modeling and the benefits for space geodetic techniques. *Journal of Geodesy*, *85*(12), 887–907. https://doi.org/10.1007/s00190-011-0508-5

Jakowski, N., Mayer, C., Hoque, M. M., & Wilken, V. (2011). Total electron content models and their use in ionosphere monitoring. *Radio Science*, *46*(6). https://doi.org/10.1029/2010RS004620

Jin, S., Gao, C., Yuan, L., Guo, P., Calabia, A., Ruan, H., & Luo, P. (2021). Long-term variations of plasmaspheric total electron content from topside GPS observations on LEO satellites. *Remote Sensing*, *13*(4), 545. https://doi.org/10.3390/rs13040545

Jin, S., & Su, K. (2020). PPP models and performances from single-to quad-frequency BDS observations. *Satellite Navigation*, *1*(1), 16. https://doi.org/10.1186/s43020-020-00014-y

Kanevsky, M., Arutyunyan, R., Bolshov, L., Demyanov, V., & Maignan, M. (1996). Artificial neural networks and spatial estimation of Chernobyl fallout. *Geoinformatics*, *7*(1–2), 5–11. https://doi.org/10.6010/geoinformatics1990.7.1-2_5

Kashcheyev, A., & Nava, B. (2019). Validation of NeQuick 2 Model Topside Ionosphere and Plasmasphere Electron Content Using COSMIC POD TEC. *Journal of Geophysical Research: Space Physics*, *124*(11), 9525–9536. https://doi.org/10.1029/2019JA026971

Kotova, G. A. (2007). The Earth's plasmasphere: State of studies (a Review). *Geomagnetism and Aeronomy*, *47*(4), 409–422. https://doi.org/10.1134/S0016793207040019

Lazzaro, D., & Montefusco, L. B. (2002). Radial basis functions for the multivariate interpolation of large scattered data sets. *Journal of Computational and Applied Mathematics*, *140*(1), 521–536. https://doi.org/10.1016/S0377-0427(01)00485-X

Lee, H. B., Jee, G., Kim, Y. H., & Shim, J. S. (2013). Characteristics of global plasmaspheric TEC in comparison with the ionosphere simultaneously observed by Jason-1 satellite. *Journal of Geophysical Research: Space Physics*, *118*(2), 935–946. https://doi.org/10.1002/jgra.50130

Moody, J., & Darken, C. J. (1989). Fast learning in networks of locally-tuned processing units. *Neural Computation*, *1*(2), 281–294. https://doi.org/10.1162/neco.1989.1.2.281

Munyati, C., & Sinthumule, N. I. (2021). Comparative suitability of ordinary kriging and inverse distance weighted interpolation for indicating intactness gradients on threatened savannah woodland and forest stands. *Environmental and Sustainability Indicators*, *12*, 100151. https://doi.org/10.1016/j.indic.2021.100151

Niros, A. D., & Tsekouras, G. E. (2012). A novel training algorithm for RBF neural network using a hybrid fuzzy clustering approach. *Fuzzy Sets and Systems*, *193*, 62–84. https://doi.org/10.1016/j.fss.2011.08.011

Oliver, M. A., & Webster, R. (1990). Kriging: A method of interpolation for geographical information systems. *International Journal of Geographical Information Systems*, *4*(3), 313–332. https://doi.org/10.1080/02693799008941549

Panda, S. K., Haralambous, H., Moses, M., Dabbakuti, J. R. K. K., & Tariku, Y. A. (2021). Ionospheric and plasmaspheric electron contents from space-time collocated digisonde, COSMIC, and GPS observations and model assessments. *Acta Astronautica*, *179*, 619–635. https://doi.org/10.1016/j.actaastro.2020.12.005

Pedatella, N. M., Forbes, J. M., Maute, A., Richmond, A. D., Fang, T. W., Larson, K. M., & Millward, G. (2011). Longitudinal variations in the F region ionosphere and the topside ionosphere-plasmasphere: Observations and model simulations. *Journal of Geophysical Research*, *116*(A12), A12309. https://doi.org/10.1029/2011JA016600

Pedatella, N. M., & Larson, K. M. (2010). Routine determination of the plasmapause based on COSMIC GPS total electron content observations of the midlatitude trough. *Journal of Geophysical Research*, *115*(A9), A09301. https://doi.org/10.1029/2010JA015265

Seo, Y., Kim, S., & Singh, V. (2015). Estimating spatial precipitation using regression kriging and artificial neural network residual kriging (RKNNRK) hybrid approach. *Water Resources Management*, *29*(7), 2189–2204. https://doi.org/10.1007/s11269-015-0935-9

Shi, Q., Jin, S., & Li, L. (2023). Daily plasmaspheric TEC variations from COSMIC GPS observations based on RBF neural network-kriging method [Dateset]. *Figshare*. Retrieved From https://doi.org/10.6084/m9.figshare.22132127

Shim, J. S., Jee, G., & Scherliess, L. (2017). Climatology of plasmaspheric total electron content obtained from Jason 1 satellite. *Journal of Geophysical Research: Space Physics*, *122*(2), 1611–1623. https://doi.org/10.1002/2016JA023444

Su, K., Jin, S., Jiang, J., Hoque, M., & Yuan, L. (2021). Ionospheric VTEC and satellite DCB estimated from single-frequency BDS observations with multi-layer mapping function. *GPS Solutions*, *25*(2), 68. https://doi.org/10.1007/s10291-021-01102-5

Takka, E., Belhadj-Aissa, A., & Kimouche, H. (2018). An end-to-end approach for near real time ionosphere monitoring over mid-latitudes from GPS data using kriging interpolation and IGS products. In *Paper presented at 2018 IEEE/ION position, location and navigation symposium*. PLANS.

Yizengaw, E., Moldwin, M. B., Galvan, D., Iijima, B. A., Komjathy, A., & Mannucci, A. J. (2008). Global plasmaspheric TEC and its relative contribution to GPS TEC. *Journal of Atmospheric and Solar-Terrestrial Physics*, *70*(11), 1541–1548. https://doi.org/10.1016/j.jastp.2008.04.022

Yue, X., Schreiner, W. S., Hunt, D. C., Rocken, C., & Kuo, Y.-H. (2011). Quantitative evaluation of the low Earth orbit satellite based slant total electron content determination. *Space Weather*, *9*(9). https://doi.org/10.1029/2011SW000687

Zhang, B. (2016). Three methods to retrieve slant total electron content measurements from ground-based GPS receivers and performance assessment. *Radio Science*, *51*(7), 972–988. https://doi.org/10.1002/2015RS005916

Zhang, M., Liu, L., Wan, W., & Ning, B. (2016). Variation of the plasmaspheric electron content derived from the podTEC observations of COSMIC LEO satellites to GPS signals. *Chinese Journal of Geophysics (in Chinese)VL -*, *59*(1), 1–7. https://doi.org/10.6038/cjg20160101

Zhang, M., Liu, L., Wan, W., & Ning, B. (2017). Comparison of the observed topside ionospheric and plasmaspheric electron content derived from the COSMIC podTEC measurements with the IRI_Plas model results. *Advances in Space Research*, *60*(2), 222–227. https://doi.org/10.1016/j.asr.2016.10.025

Zhong, J., Lei, J., Dou, X., & Yue, X. (2016). Assessment of vertical TEC mapping functions for space-based GNSS observations. *GPS Solutions*, *20*(3), 353–362. https://doi.org/10.1007/s10291-015-0444-6

Zhong, J., Lei, J., Wang, W., Burns, A. G., Yue, X., & Dou, X. (2017). Longitudinal variations of topside ionospheric and plasmaspheric TEC. *Journal of Geophysical Research: Space Physics*, *122*(6), 6737–6760. https://doi.org/10.1002/2017JA024191